Experimental Validation of Thermophoretic and Bend Nanoparticle Loss for a Regulatory Prescribed Aircraft nvPM Sampling System

Eliot F. Durand[a]*, Andrew P. Crayford[a], Mark Johnson[b]

[a]*Cardiff School of Engineering, Cardiff University, Wales, UK, CF24 3AA*

[b]*Rolls-Royce, plc., Sin A-37 PO Box 31, Derby, UK, DE24 8BJ*

Address correspondence to Eliot Durand, Cardiff University, School of Engineering, Queen's Buildings, 14-17 The Parade, Cardiff, CF24 3AA, UK. E-mail: DurandEF@cardiff.ac.uk

Experimental Validation of Thermophoretic and Bend Nanoparticle Loss for a Regulatory Prescribed Aircraft nvPM Sampling System

Abstract

Aircraft gas turbine engines produce ultrafine PM which has been linked to local-air-quality and environmental concerns. Regulatory sampling and measurement standards were recently introduced by ICAO to mitigate these emission of non-volatile PM (nvPM). Currently, reported nvPM emissions can significantly under-represent engine exit concentrations due to particle loss. A System-Loss-Tool (SLT) has been proposed to correct for particle loss in the standard sampling and measurement system permitting an estimation of engine exit concentrations for airport environment inventories.

Thermophoretic and bend particle loss mechanisms are predicted in the SLT using expressions derived from the literature, which are not in all cases empirically validated to conditions representative of aircraft nvPM exhaust sampling methodologies. In this study, thermophoretic (T_{gas}≤910°C) and coiling-induced (≤3960°) particle loss were measured using sampling variables relevant to aerospace certification. Experiments were performed using laboratory generated solid particles (fractal graphite, cubical salt and spherical silica) bounding the upper and lower limits of aircraft soot morphology (i.e. particle effective density, mass-mobility exponent, primary-particle-size). These were aerodynamically classified using a Cambustion Aerodynamic-Aerosol-Classifier (AAC) at electrical-mobility diameters ranging from 30–140 nm.

The AAC was shown to efficiently classify salt and silica particles, producing monomodal distributions ≥25 nm electrical-mobility GMD, whilst classifying fractal graphite >40 nm electrical-mobility GMD (calculated as d_a≥20 nm) albeit generally displaying larger GSD's. Thermophoretic loss at ΔT_{gas} of 0–880 K correlated well with the SLT for non-fractal particles with losses ≤39.2% measured, with higher depositions observed for graphite (4.1%) considered insignificant compared to overall measurement uncertainty. Coiling a 25 m sample line in compliance with ICAO standards induced negligible additional particle loss at flowrates relevant of aircraft exhaust sampling, in agreement with SLT-predicted bend losses. However, additional losses were witnessed at lower flowrates (≤13% at 30 nm), attributed to secondary flow diffusion loss induced by the coiling.

Keywords: Particle transport, Particle loss, Aircraft nvPM, Aircraft regulation, Thermophoretic loss, Bend loss, Particle generation, Particle classification

Nomenclature

Symbol	Unit	Definition
C_c	-	Cunningham correction factor
C_m (=1.14)	-	Momentum correction factor
C_s (=1.17)	-	Slip correction factor
C_t (=2.18)	-	Thermal correction factor
C_p	[J/K]	Gas specific heat capacity
d_a	[m]	Aerodynamic diameter
d_m	[m]	Electrical-mobility diameter
D	[m^2/s]	Diffusion coefficient
D_{50}	[%]	50% efficiency cut-off diameter
D_{90}	[%]	90% efficiency cut-off diameter
D_{tube}	[m]	Tube inner diameter
D_m	-	Mass-mobility exponent
D_{pp}	[nm]	Primary particle diameter
h	[W/m^2/K]	Heat transfer coefficient
k_m	-	Mass-mobility pre-factor
K_{th}	-	Thermophoretic coefficient
Kn	-	Knudsen number
k_g	[W/m/K]	Gas thermal conductivity
k_p	[W/m/K]	Particle thermal conductivity
L_{tube}	[m]	Tube length
Pr	-	Prandtl number
Q	[m^3/s]	Volumetric flowrate at STP
Re	-	Reynolds number
R^2	-	Coefficient of determination
Sc	-	Schmidt number
Stk	-	Stokes number
T	[K]	Temperature
ρ_0	[kg/m^3]	unit density (=1000)
ρ_p	[g/cm^3]	Particle density
θ	Radians	Angle of bends

1. Introduction

Aircraft gas turbine engines emit ultrafine Particulate Matter (PM) with number-weighted geometric mean diameters (GMD) <100 nm into the atmosphere (Boies et al., 2015; Delhaye et al., 2017; Durdina et al., 2014; Lobo et al., 2015a). Aircraft near-plume PM is comprised of a mixture of elements typically classified into two groups namely semi-volatile particles (predominantly sulfates, unburnt hydrocarbons and lubrication oils (Fushimi et al., 2019; Kittelson, 1998)) and non-volatile fractal aggregates (Boies et al., 2015; Saffaripour et al., 2019) defined as any particle exiting a gas turbine engine that is found in the gas phase at a temperature of ≥350°C (ICAO, 2017) and consisting essentially of solid carbonaceous particles (i.e. soot/black carbon). Aircraft PM is the main anthropogenic particulate source in the upper atmosphere and has recently been linked to air quality issues in the vicinity of airports resulting in potential health impacts (Jonsdottir et al., 2019; Masiol and Harrison, 2014). Due to the small particle size, combustion generated ultrafine PM has been shown to efficiently penetrate the respiratory tract and reach the human brain which coupled with the delivery of toxic semi-volatile coatings has raised health concerns (Steiner et al., 2016; Weichenthal et al., 2019).

In response to the aforementioned concerns, the International Civil Aviation Organization (ICAO) has recently introduced a new global non-volatile PM (nvPM) emission reporting standard to regulate emitted concentrations of aircraft nvPM. This new standard is relevant for both in-production and new gas turbine engines (>26.7 kN) from 1st January 2020 (ICAO, 2017). Due to the hostile environment at aircraft engine exit, a long sampling system is used to transport the exhaust sample to the real-time measurement analyzers. To enable repeatable measurement of nvPM, this system is also required to dilute, cool and condition the aerosol prior to measurement. As has been previously reported (Baron et al., 2011; Giechaskiel, 2012; Hinds, 1998), there are numerous mechanisms by which the sampled ultrafine nvPM can be lost to the sampling system prior to measurement.

To permit the systematic reporting of aircraft nvPM, an ICAO standard sampling and measurement methodology was developed based on the findings of numerous international collaborative programs (Crayford and Johnson, 2013; Lobo et al., 2015b, 2020; Petzold et al., 2011). The sampling protocols for the regulation of aircraft nvPM emissions (ICAO, 2017) specify a sampling system of up to 35 m line length which, coupled with relatively small GMDs of nvPM often witnessed from gas turbines, result in significant particle loss before measurement at the nvPM mass and number instruments. Due to size-dependent particle loss mechanisms, losses of nvPM in a standard sampling system are estimated to be as high as 90% for number concentration and up to 50% for mass concentration across representative engines and powers (ICAO, 2017; SAE international, 2019). To facilitate a direct comparison of emitted aircraft nvPM required for air quality inventory, it is therefore necessary to determine nvPM concentrations at the engine exit rather than at the end of the sampling system. However, only particle number and mass concentration measurements are currently prescribed, hence reported nvPM emissions are corrected only for size-independent thermophoretic particle loss in the collection section. To account for size-dependent particle losses, a system loss and counting efficiency correction methodology has recently been proposed for both nvPM number and mass by the SAE E-31 committee as an Aerospace Recommended Practice (SAE international, 2019). This methodology is also described for the reporting of nvPM number and mass correction factors (ICAO 2017, Appendix 8).

Particle transport efficiency in an ICAO standard sampling system is estimated using the United Technologies Research Centre (UTRC) particle transport model published with the SAE E-31 Aerospace Information Report 6504 (SAE international, 2017). The UTRC model predicts particle transport efficiency by coupling flow characteristics to gas and particle properties over a range of particle sizes through user-defined sampling system segments. The PM transport is modelled using equations derived from the literature and considers five loss mechanisms

namely: diffusion, thermophoresis, electrostatic, inertial and bend. Given the length (≤35 m) of an ICAO standard sampling system and the elevated temperature at the exhaust of a gas turbine which is typically up to 700°C (Lobo et al., 2015b; SAE international, 2018), it can be shown that the main deposition mechanisms for ultrafine aircraft nvPM are thermophoresis and diffusion. Previous studies have investigated specific loss mechanisms of nanoparticles, however, variables relevant to aerospace nvPM morphology, sampling and transport have not always been isolated. Thermophoretic deposition (Lin et al., 2008; Messerer et al., 2003; Muñoz-Bueno et al., 2005; Romay et al., 1998; Shimada et al., 1993; Tsai et al., 2004) has previously been described, however to the author's knowledge, little validation work has been performed at temperatures representative of gas turbine exhaust (≥450°C), particularly using fractal particles. Limited studies have investigated thermophoretic losses using soot-like particles (Messerer et al., 2003), for limited temperature differentials (<110°C). Conversely, high temperature thermophoretic measurements at furnace temperatures up to 900°C have been conducted (Shimada et al., 1993), however in this case non-fractal particles were utilized.

To minimize bend losses, the current civil aviation regulation (ICAO, 2017) prescribes that sample lines should be as "straight through" as practical. When line bending is unavoidable, it is described that bends must have radii greater than ten times the internal diameter of the lines and that any bend in the sample line has a minimum coiled radius of 0.5 m. Again, limited experimental validation of particle loss in pipes have been performed with non-fractal particles (Kumar et al., 2008; Tsai, 2015; Yin and Dai, 2015) and using soot particles (Crayford and Johnson, 2012) in a nominally straight sample line.

The motivation for this research is to better understand the uncertainty associated with aircraft nvPM sampling system loss correction methodology as prescribed by ICAO, by further validating the UTRC model equations in terms of thermophoretic and bend loss at sampling conditions and temperatures representative of aircraft exhaust which have not previously been

experimentally validated in the literature. Thermophoretic and bend loss experiments were performed using laboratory generated graphite, silica and salt particles classified with a Cambustion Aerodynamic Aerosol Classifier (AAC) spanning nvPM sizes relevant to aircraft particle loss (30 – 140 nm). Reported aircraft nvPM GMDs typically range from 15 – 50 nm with GSDs of 1.5 – 1.9 corresponding to particles ranging between 10 – 200 nm (Lobo et al., 2015a; Saffaripour et al., 2019; Zhang et al., 2019). The measured GMD is typically larger (i.e. >30 nm) at higher thrusts corresponding to a major fraction of the ICAO regulated Landing-Take-Off cycle. Given the challenges associated with the generation of highly concentrated well-characterized particles <30 nm, this study investigated particle loss between 30 – 140 nm to inform size-independent thermophoretic loss, and bend losses which in theory only impact larger particles and hence largely the nvPM mass measurement. Diffusion loss as estimated in the SLT, is a major loss mechanism for nvPM number, and predominantly impacts nvPM <30 nm, but is not the focus of this study.

The measured empirical data was subsequently compared to the UTRC model predictions. The impact of particle morphology (fractal graphite, spherical silica, cubical salt) on these loss mechanisms was also assessed. Furthermore, aircraft engine manufacturers utilize combustion rigs, for emission research, where the probe inlet can reach temperatures of up to 1850°C, as such the probe is typically water-cooled for protection and to quench reactions within the sampled aerosol. Further understanding of thermophoretic loss at higher temperature gradients is not only relevant for correcting nvPM certification measurements but also towards the interpretation of nvPM emissions data from combustor rigs.

2. Experimental Methods

To perform the PM loss experiments described in this study, particles were generated and introduced into particle loss specific test sections. Penetration efficiencies through the test

sections were then derived from differential measurement of particle number concentrations at the inlet and outlet. A schematic representation of the experimental set-up employed is given in **Figure 1**.

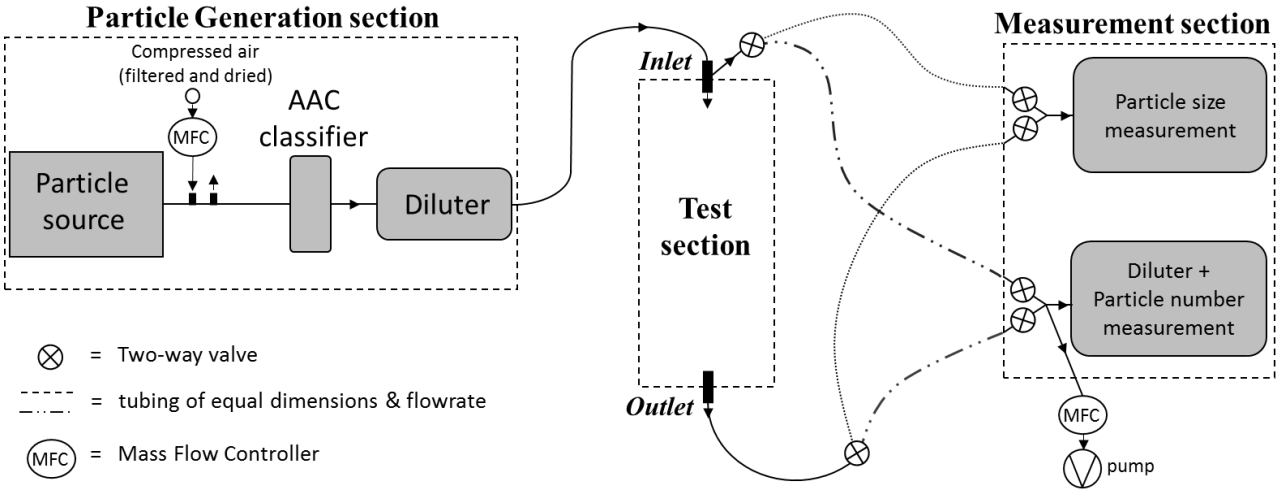

Figure 1: Schematic representation of experimental setup for thermophoretic and bend particle loss laboratory experiments

2.1. Particle generation

Nanoparticles (silica, salt and graphite) covering a range of morphologies were generated using either nebulization or a spark discharge, with their generation technique and physical properties listed in **Table 1**. The three particle types used were selected to bound the upper and lower limits of key aircraft soot morphological properties (i.e. mass-mobility exponent, effective density, primary particle size) with non-fractal salt and silica around double the density of typical fresh denuded combustion soot (Olfert and Rogak, 2019) at 20 nm and highly fractal graphite about half the density at 200 nm, as highlighted in **Figure 2**.

Table 1: Properties of the particles used in the loss experiments

Material type	Particle diameter [nm]	Generation technique	Melting point [°C]	Morphology
Silica (SiO_2) suspensions from Nanocomposix	50, 100, 180	Nebulization of suspensions	1700	Spherical

Salt from a saline solution (0.9% NaCl w/v)	10-200	Nebulization of solutions	800	Cubical (Park et al., 2009)
Graphite (Carbonaceous nanoparticles)	20-200	Spark Discharge (Palas GFG-1000)	≥3600	Fractal aggregates (Brugière et al., 2014)

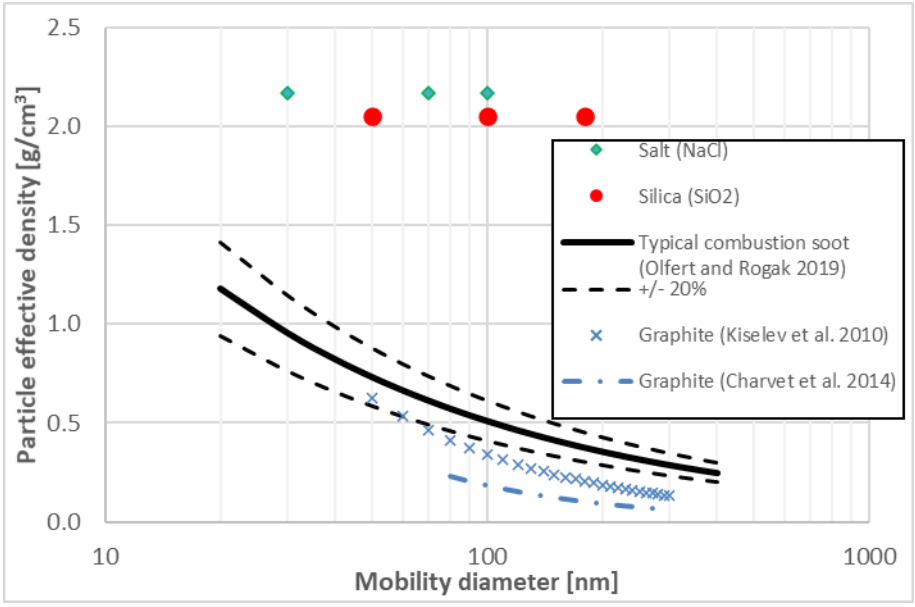

Figure 2: Effective density of Graphite, Salt, Silica compared to that of typical denuded soot from common combustion sources

An axial dilution stage was employed prior to classification to ensure full evaporation of the liquid droplets generated by the nebulization techniques (Hinds, 1998). Additionally, an ejector dilution stage (Palas VKL 10E) was used after particle classification to control particle concentration whilst also ensuring satisfactory mixing, sufficient flowrate availability and consistent pressure in the test section independent of flowrate and particle generation method. Furthermore, the tubing length between diluter outlet and the test section inlet was sufficiently long to ensure the sample flow was fully developed limiting any impact of entrance effects (Kreith et al., 2012).

For both the silica and salt nebulization, a Topas ATM-226 collision nebulizer was used. The resulting aerosol after evaporation was shown to be suitable for the generation of solid particles at sizes of 30 –140 nm. The small liquid droplets exiting the ATM-226 (GMD ≤200 nm)

minimized Non-Volatile Residual (NVR) contamination resulting from dissolved impurities (Fissan et al., 2014; Jeon et al., 2016; Park et al., 2012), with NVR peaks witnessed being <30 nm, limiting their impact on the particle loss experiments presented here. Nebulized Ultrapure water (ASTM type 1), manufactured using a 'Sartorius arium comfort' system, was found to produce NVR particles <20 nm at concentrations of $\approx 10^4$ particles/cm^3. Hence, it was demonstrated as suitable for the nebulization of the relatively larger silica nanoparticle suspensions.

A PALAS GFG-1000 spark-discharge generator was used to produce fractal graphite particles. When compared with other soot sources (e.g. diffusion flame burners, Diesel engines), these graphite particles are composed of relatively smaller primary particles ($D_{pp} \approx 5–15$ nm) with a lower mass-mobility exponent (Charvet et al., 2014; Gysel et al., 2012), resulting in a relatively lower effective density than typical combustion soot as depicted in **Figure 2** (Olfert and Rogak, 2019; Saffaripour et al., 2019). PALAS GFG-1000 generated graphite was also utilized in this study as high concentrations of solid carbonaceous particles could be produced at a large range of sizes (PALAS GmbH), minimizing measurement uncertainty associated with volatilization of organic species during the high temperature thermophoretic particle loss experiments.

To facilitate the study of size-dependent particle loss mechanisms, monomodal nanoparticle distributions were produced using a Cambustion AAC aerodynamic classifier (Tavakoli and Olfert, 2013; Tavakoli et al., 2014). Previous authors have used Differential Mobility Analyzers (DMA) (Cheng et al., 2002; Giechaskiel et al., 2009; Lyyränen et al., 2004; Romay et al., 1998) to classify the generated aerosol which are typically polydisperse or multimodal. In contrast to a DMA, the AAC classifies particles according to their aerodynamic diameter rather than electrical-mobility diameter, as is also the case of the TSI APS and the Dekati ELPI. The AAC uses centrifugal force and relaxation time to classify particles and hence has better transmission efficiencies, 2 to 5 times higher, than electrostatic classifiers providing higher concentrations

of test aerosols for the loss measurements. The AAC classification technique also removes uncertainties associated with multiple-charging artefacts witnessed using DMA selection (Johnson et al., 2018).

When atomizing and classifying suspensions or solutions, a drier is typically used prior to a DMA (Cheng et al., 2002; Muñoz-Bueno et al., 2005; Romay et al., 1998; Tsai et al., 2004) to maintain a low Relative Humidity (RH) resulting in rapid droplet evaporation whilst ensuring the sampled flow is of a similar RH to the sheath flow. Dilution was used in this study to dry the nebulized aerosol to a suitably low RH (<50%) ensuring total evaporation of liquids prior to the AAC.

2.2. Penetration efficiency measurement

Particle size distribution and number concentrations were sequentially measured at both the inlet and outlet of the test section using a suitably calibrated Cambustion Differential Mobility Spectrometer (DMS-500) and AVL Advanced Particle Counter (APC). Two-way full-bore valves and a flow-controlled pump (**Figure 1**), were used to provide continuous and matched sample flows at both inlet and outlet of the test section, with the DMS-500 and APC alternating between the two positions. This technique was employed to remove uncertainties associated with the use of multiple analyzers (drift, calibration, accuracy etc.), hence simplifying the calculation of penetration efficiency. All sample lines were electrically conductive (stainless steel & conductive silicone tubing) and grounded to minimize electrostatic loss (Giechaskiel, 2012; Tsai, 2015). The sample line dimensions and flowrates were matched to limit and make consistent the associated particle loss mechanisms from test section inlet and outlet to the measurement analyzer. Hence simple division facilitated the determination of particle loss in the test section.

The APC consists of a catalytic stripper based Volatile Particle Remover (VPR) and n-butanol

TSI 3790E Condensation Particle Counter (CPC) (SAE international, 2018). In compliance with aviation measurement protocols the CPC exhibited ≥ 50% and 90% cut-off diameters (D_{50}, D_{90}) of 10 nm and 15 nm respectively. The DMS-500 measures particle electrical mobility size distributions (5-1000 nm) using a unipolar diffusion charger and classifier column. Suitable calibration files (spherical or aggregate) are required to invert measured currents on the electrometer rings and predict the particle number concentration and size data (Biskos et al., 2005; Hagen et al., 2009). The particle size data was used to determine potential changes in particle morphology (e.g. particle collapsing or evaporation) during the thermophoretic experiments, by assessing changes in GMD and Geometric Standard Deviation (GSD) pre- and post-test section. The monitoring of GMD and GSD by the DMS-500 also permitted to determine if oxidation (from graphite or the stainless-steel bar) was impacting the derived penetration efficiency. To prevent oxidation during the highest temperature cases, Nitrogen was used as a diluent with comparisons of Nitrogen and Air conducted at lower temperatures to ensure this did not impact other loss mechanisms (Durand, 2019). For the data presented in this study, the inlet to outlet particle size distribution fluctuations were 3.1±2.7% for GMD and 1.5±1.7% for GSD.

Experimental penetration efficiencies were independently quantified using both the particle number concentrations reported by both the APC and DMS-500 analyzers. This was achieved by dividing analyzer specific particle number concentrations measured at the outlet of the test section by those measured immediately prior at the inlet. Number concentrations were derived from 30-second averages taken at a stable condition (coefficient of variation <3%) at an acquisition rate of 1 Hz. Time between the sequential measurements was limited as low as practicable (30 s – 2 min) to minimize uncertainties associated with particle generator and dilution drift.

It is noted that this study was performed over several days with cleanliness checks performed

regularly to ensure the integrity of the test and sampling pipework and analyzers (i.e. measuring no signal during zero checks).

2.3. Particle loss test sections

Two different test sections were utilized, the first to measure thermophoretic loss and the second diffusion and bend losses. The particle loss mechanisms were investigated at three sample flowrates of 8, 16 and 24 standard L/min (i.e. sL/min where standard refers to 0°C and 101.325 kPa (ICAO, 2017)) covering laminar to transition/turbulent flow conditions.

2.3.1. Thermophoretic loss test section

A test section for the measurement of thermophoretic losses was designed as depicted in **Figure 3**, being constructed in three zones namely:

- Ambient segment - consisted of a 0.6 m water-cooled tube in tube heat exchanger (WHX1), this prevented heat from transferring from the hotter zones to the particle generation section.

- Heating segment - The heating segment consisted of a 1 m x 50 mm Outer Diameter (OD) Grade RA330 Stainless Steel (working temperature 1148°C before oxidation), thick-walled tube of 8 mm Internal Diameter (ID), pre-heated by three 750 W Watlow clamp heaters affording temperatures ≤600°C. The tube was further heated by a tube furnace (Severn furnace limited TF825 - 1.5 kW) enabling temperatures of ≤1000°C. Numerous thermocouples were fitted on the outer walls of the tube to control the clamp heaters and monitor the tube wall temperature.

- Cooling segment - composed of a 1.7 m counterflow water cooled tube in tube heat exchanger (WHX2) used to cool the hot aerosol to approximately ambient (<30°C),

forcing thermophoretic particle deposition.

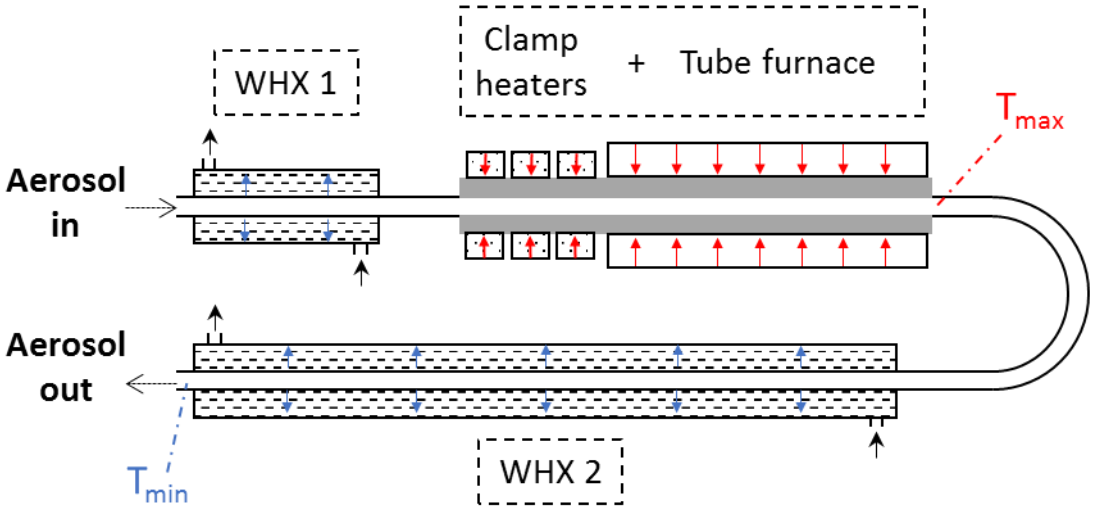

Figure 3: 2-D Schematic representation of the thermophoretic experiment test section

The cooling and heating lengths were designed using theoretical predictions (Baron et al., 2011; Kreith et al., 2012) assuming localized steady state conditions and that heat from the tube to the flowing gas stream was transferred by forced convection (radiation effects neglected). This ensured the required gas temperatures were reached in minimal line lengths hence minimizing non-thermophoretic loss. A 180° bend was used between the heated and cooling segment of the thermophoretic test section to minimize the physical distance between the inlet/outlet of the test section, this allowed short nominally identical line lengths to the measurement instruments. The single bend was designed in line with ICAO recommendations (ICAO, 2017), with the bend radius greater than 10 times D_{tube}, ensuring negligible bend loss which was confirmed during the commissioning of the test section.

2.3.2. Bend loss test section

The test section for measuring bend particle loss consisted of a heated 25 m sample line constructed of flexible 8 mm ID antistatic PTFE (Winkler series WAMX1537), which conforms to the specifications of ICAO annex 16 Volume II: Appendix 7 (ICAO, 2017). Bend loss was

assessed by comparing measured particle penetration efficiencies for two sample line settings:

(1) A ‘straight’ case, which included one large diameter coil to facilitate the inlet and outlet being spatially close, limiting the requirement of excessively long connecting sample lines to the measurement analyzers (total bends <720°).

(2) A ‘coiled’ case where the same 25 m line was coiled eleven times (total bends≈3960°) at a diameter of ≈0.65 m (curvature ratio=81.25), representing the tightest bend that was achievable with the heated sample line construction.

When sequentially measuring particles at the inlet and outlet of the test section, to account for the additional associated pressure drop of the sample line and maintain equal flowrates to the DMS-500, two nominally identical 1 μm cyclones fitted with different restrictors were used at the inlet and exit of the test section.

3. Theoretical Particle Loss Mechanisms

3.1. UTRC particle transport model theory

Theoretical penetration efficiencies were estimated using the UTRC particle transport model. The expressions used in the UTRC model to approximate thermophoretic and bend loss are introduced below with full details of the specific loss mechanisms presented elsewhere (Baron et al., 2011; Hinds, 1998).

Thermophoresis: The thermophoretic deposition efficiency is estimated in the UTRC model using an expression derived from thermophoretic deposition measurements at temperatures of 300 to 425 K (<150°C) using NaCl and PSL particles (Romay et al. (1998)):

$$\eta_{\text{thermo}} = \left(\frac{T_{\text{wall}} + \left(T_{\text{gas}} - T_{\text{wall}}\right) \exp\left(\frac{-\pi \times D_{\text{tube}} \times h \times L}{\rho_p \times Q \times C_p}\right)}{T_{\text{gas}}} \right)^{\text{Pr}\times K_{\text{th}}} \quad (1)$$

Whereby the thermophoretic coefficient K_{th} is determined using:

$$K_{\text{th}} = \frac{2 \times C_S \times C_C}{1 + 3C_m \times \text{Kn}} \left(\frac{\frac{k_{\text{g}}}{k_{\text{p}}} + C_t \times \text{Kn}}{1 + \frac{2 \times k_{\text{g}}}{k_{\text{p}}} + 2C_t \times \text{Kn}} \right) \quad (2)$$

For the case of aviation relevant particles, effective density (ρ_{p}) is currently assumed as 1 g/cm^3 (Durdina et al. 2014) and the particle thermal conductivity (k_{p}) 0.2 W/(m.K) (Messerer, Niessner, and Pöschl 2003).

For the case of aviation soot a simplified version for thermophoretic correction (k_{thermo}) has been proposed (Giechaskiel, 2012; SAE international, 2018), which only requires knowledge of the engine exhaust gas temperature (T_{EGT}) and sample line wall temperature (T_{wall}), as given by:

$$k_{\text{thermo}} = \left(\frac{T_{\text{max}}\,[\text{K}]}{T_{\text{min}}[\text{K}]} \right)^{Pr.K_{\text{th}}} \approx \left(\frac{T_{\text{ETG}}[\text{K}]}{T_{\text{wall}}[\text{K}]} \right)^{0.38} \quad (3)$$

Bends: The deposition efficiency of nanoparticles caused by bends is estimated in the UTRC model using two equations depending on the witnessed Reynolds number. These equations were derived from experiments in a 90° bend using liquid particles (Crane and Evans, 1977; Pui et al., 1987), as given by:

$$\eta_{\text{bend}} = 1 - \text{Stk} \times \theta \text{ for Re} < 5000 \quad (4)$$

$$\eta_{\text{bend}} = \exp[-2.823 \times \text{Stk} \times \theta] \text{ for Re} > 5000 \quad (5)$$

3.2. Estimation of penetration efficiencies

The UTRC model predicts total particle loss in a given sampling system by combining the individual loss mechanisms (thermophoretic, diffusion, electrostatic, bend & inertial) through

different user defined segments as represented in **Figure 4**.

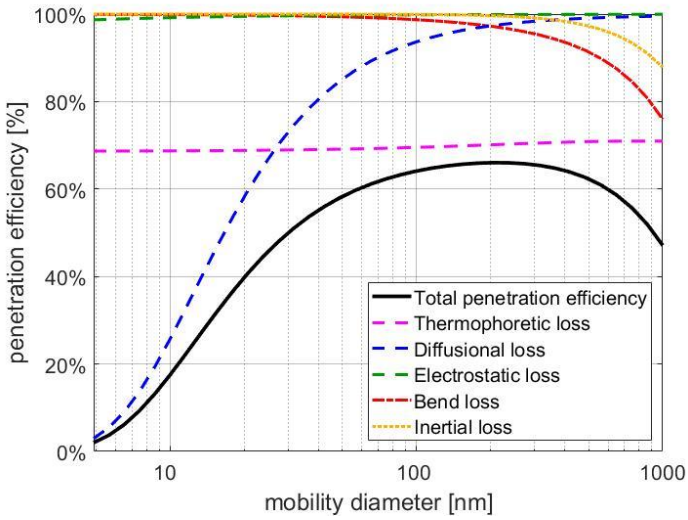

Figure 4: Example of nanoparticle penetration efficiency in a typical ICAO standard sampling system estimated using the UTRC model

Theoretical penetration efficiencies of the two aforementioned test sections were estimated using the UTRC model. However, to account for non-monodispersed aerosols, the size specific UTRC derived penetration function was applied to the measured particle size distribution at the inlet of the test section. This resulted in a size distribution predicted at the test section outlet, which when compared to that measured at the inlet was used to derive a theoretical penetration efficiency.

To estimate theoretical thermophoretic losses (Equation **(1**&**3)**), the maximum (i.e. hot) and minimum (i.e. cold) aerosol temperatures were required. These temperatures could not be directly measured using an intrusive immersed thermocouple during the particle loss experiments due to the associated impaction loss (Romay et al., 1998). Hence, the aerosol T_{max} and T_{min} were empirically determined with an immersed traceably calibrated thermocouple (1 m long, 6 mm OD TC direct ceramic twin bore insulated thermocouple) post particle loss experiment at the same conditions employed for loss determination.

4. Results and Discussion

4.1. Particle size distributions

As discussed previously, generated aerosols of silica, salt, and graphite were classified according to their aerodynamic diameter using a Cambustion AAC. Three distinct characterized distributions representing small, medium and large GMDs were selected for each experiment and particle type by controlling the AAC resolution (i.e. sheath flow to aerosol flow ratio) and aerodynamic diameter (d_a) parameters, as given in **Table 2**. Classification setpoints were optimized to produce sufficient concentrations of particles for the measuring analyzers and narrowest peak (i.e. smallest GSD) for size-dependent particle loss characterization. However, as particle size distributions were seen to fluctuate daily, the AAC classification setpoints (i.e. resolution and d_a) were adjusted regularly to achieve the targeted specific GMD and GSD prior to each experiment. Variables in the dilution, aerosol generator and classifier setpoints were also used to ensure flowrates and particle number concentrations remained sufficiently high ($>10^5$ particles/cm^3 at test section inlet) for accurate measurement by both the DMS-500 and APC. The GMD and GSD of the size distributions entering the test-sections are presented in **Table 2**.

The optimized AAC-classified particle size distributions were seen to be relatively broader (GSD: 1.2 –1.9) in electrical-mobility space when compared with typical DMA classification. However, the AAC is known to classify in aerodynamic space in which distributions are assumed to be much narrower. While this shouldn't affect the size-independent thermophoresis study, it is suggested that aerodynamic space may be more suitable than electrical mobility space to investigate bend deposition.

Table 2: AAC parameters & classified particle electrical-mobility GMD and GSD used to investigate particle loss in test sections

		AAC 'small' setting	AAC 'medium' setting	AAC 'large' setting
Silica	GMD [nm]	48 - 53	84 - 94	119 - 142
	GSD	1.36 - 1.50	1.32 - 1.55	1.32 - 1.51
	AAC d_a [nm]	*105*	*180*	*300*
	AAC Sheath flow [L/min]	*4*	*5*	*3*
Salt	GMD [nm]	28 - 46	61 - 76	91 - 115
	GSD	1.23 - 1.40	1.25 - 1.44	1.33 - 1.37
	AAC d_a [nm]	*70 - 100*	*220*	*350 - 380*
	AAC Sheath flow [L/min]	*6 - 10*	*7*	*4.5 - 6*
Graphite	GMD [nm]	37 - 42	52 - 74	92 - 139
	GSD	1.60 - 1.85	1.6 - 1.89	1.37 - 1.61
	AAC d_a [nm]	*22*	*40 - 45*	*52 - 65*
	AAC Sheath flow [L/min]	*2*	*3.7 - 4.2*	*4.5 - 5*

**The AAC aerosol flow was 1.2 - 1.5 sL/min*

The classified size distributions of the three particle types, as measured at the inlet of the test sections, are presented as solid lines in **Figure 5**, where black lines indicate the small GMD range, green the medium range and blue the largest range. These classifications are taken from a broader generated particle distribution, as represented by the corresponding dashed lines. In the case of salt and graphite, a wide monomodal lognormal distribution was observed from which the distinct particle sizes were classified. However, in the case of silica, three specific standard size suspensions (50, 100 & 180 nm) were classified in order to limit the impact of NVR which were shown to display significant particle mode between 10 – 40 nm, as seen in the bi-modal distributions of the un-classified particles. As expected, sheath flow dilution in the AAC as well as diffusion and impaction losses in the classifier (Johnson et al., 2018) generally resulted in classified size distributions of lower concentrations compared to the un-classified distributions.

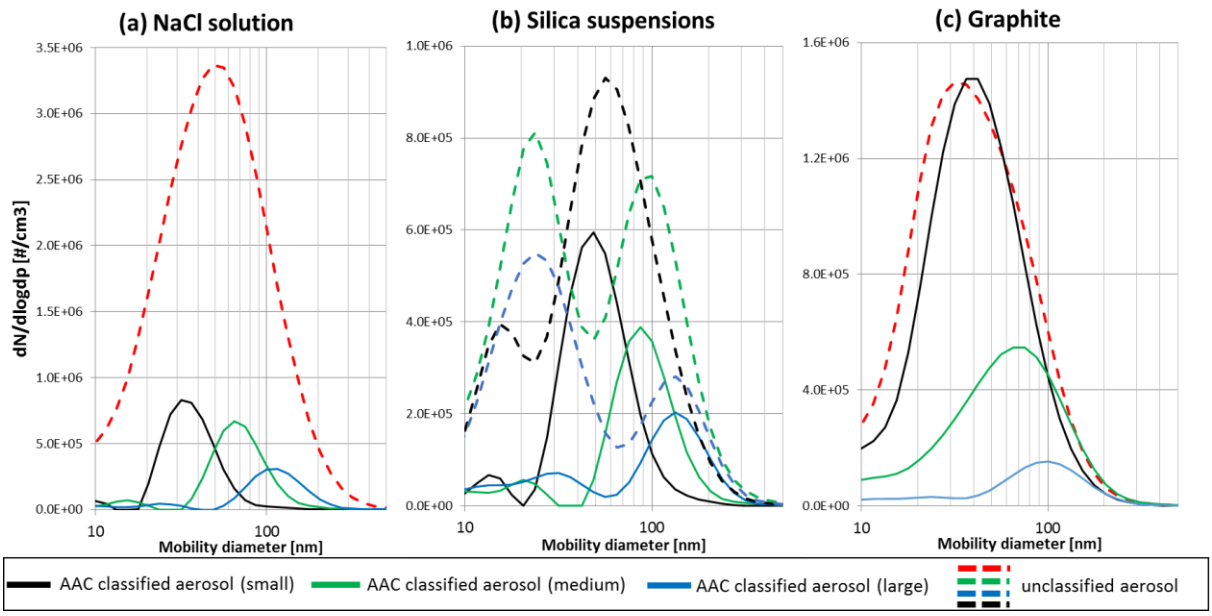

Figure 5: Particle size distributions of salt (a) and silica (b) and graphite (c) classified with an AAC at three GMDs and measured with a DMS-500

The classified distributions generally appear monodisperse but are not perfectly monomodal according to their electrical-mobility diameters, with non-negligible particle concentrations observed to the left of the main classified mode for graphite and silica. In the derivation of GMD and GSD, this data was not included in the lognormal fit which was tuned only to the main particle mode. In **Figure 5(b)**, a significant NVR artefact is observed for the case of the 180 nm classified silica distribution (blue line) at approximately 30 nm. It was found that the high diffusion loss of these small NVR particles led to inaccuracies in penetration efficiency measurement hence this data has been removed from presented datasets in this study.

When comparing particle type, graphite aerodynamic classification appears to be the least effective with larger GSD's observed (**Figure 5(c)**). This was most apparent in the smaller GMD distribution (black line) where the classified and un-classified distributions are nominally identical (i.e. 100% transmission efficiency through AAC) given the generator drift and daily fluctuation. Poor AAC classification for fractal graphite ≤40 nm electrical-mobility diameter may be explained by the lower aerodynamic diameter size classification limit of the instrument

(i.e. d_a=25 nm) (Cambustion Ltd, 2016) which requires a prescribed low resolution setting (i.e. required sheath flow ≈2 L/min at a sample flow of 1.5 L/min). Furthermore, due to the morphology of the fractal graphite, this lower 25 nm aerodynamic diameter limit corresponds to an electrical-mobility diameter of ≈40 nm. Indeed, using GFG-1000 graphite mass-mobility pre-factor (k_m=1.33E-05) and exponent (D_m=1.98) reported in the literature (Charvet et al., 2014) in equation **(6)**, an electrical-mobility diameter of 40 nm represents an equivalent aerodynamic diameter of 19.7 nm (Cambustion Ltd, 2016; Johnson et al., 2018).

$$k_m \times d_m^{(D_m-1)} \times C_c(d_m) = \rho_0 \times d_a^2 \times C_c(d_a) \quad (6)$$

It is noted that the AAC is capable higher resolutions at d_a=25 nm by reducing the sample flow to 0.3 L/min, however this was not possible in this study due to the high losses witnessed with the thermophoretic experiment and the minimum number concentration required for real-time size measurement.

For the "medium" and "large" classified graphite, the observed GSDs were generally witnessed to be larger than that of classified salt and silica at similar sizes (**Table 2**). This result can be explained by the fact that for non-spherical particles, one aerodynamic diameter can correspond to a range of particle masses with different electrical mobility diameters (Johnson et al., 2019). Additionally, the AAC spectral broadening caused by diffusion and sheath-flow disturbances is empirically corrected using a fit derived with oil droplets, but may be affected differently for fractal aggregate (Johnson et al., 2018). It is noted that AAC classification of both cubic (salt) and spherical (silica) particles was similarly efficient (i.e. similar GSDs), suggesting that the current spherical spectral broadening correction is also applicable to cubic particles. Although, small secondary peaks are visible <50 nm for the classified silica suspensions (**Figure 5(b)**), suggesting that some NVR product has a significantly different density to that of silica.

Still, the relatively poorer classification of graphite (i.e. wider GSD) is not thought to impact

the penetration efficiency results presented below given the comparable GMD and GSD measured pre- and post-test section, particularly in the case of thermophoretic loss which is shown to be size independent in the investigated size range.

4.2.Thermophoretic particle loss quantification

Thermophoretic loss was investigated for a range of particle morphologies and sizes (30 –140 nm) at increased furnace temperatures (20 –1000°C) and flowrates (8,16 and 24 sL/min) in the bespoke 'test section' detailed in **Figure 3**.

To quantify thermophoretic particle loss, it was first necessary to determine non-thermophoretic particle loss in the test section. To achieve this, penetration efficiencies were measured with the rig operated at ambient temperature (T_{max}=T_{min}=20°C). For all particle types, sizes and flowrates (49 data points), average penetration efficiencies of 97.6±1.7% were measured by the APC, in agreement with the predictions of the UTRC model (98±1.0%). Furthermore, non-thermophoretic loss theory suggests higher penetration efficiency at increased gas temperatures (flow velocity), hence for this analysis it was assumed the non-thermophoretic loss mechanisms were insignificant (i.e. lower than measurement uncertainty) and were not corrected for. It was observed that DMS-500 derived penetration data displayed more scatter (95.2±3.4%), particularly in the case of graphite particles, hence in this study only APC derived penetration efficiencies are reported. Further discussion of DMS-500 derived penetration efficiencies are presented in detail elsewhere (Durand, 2019).

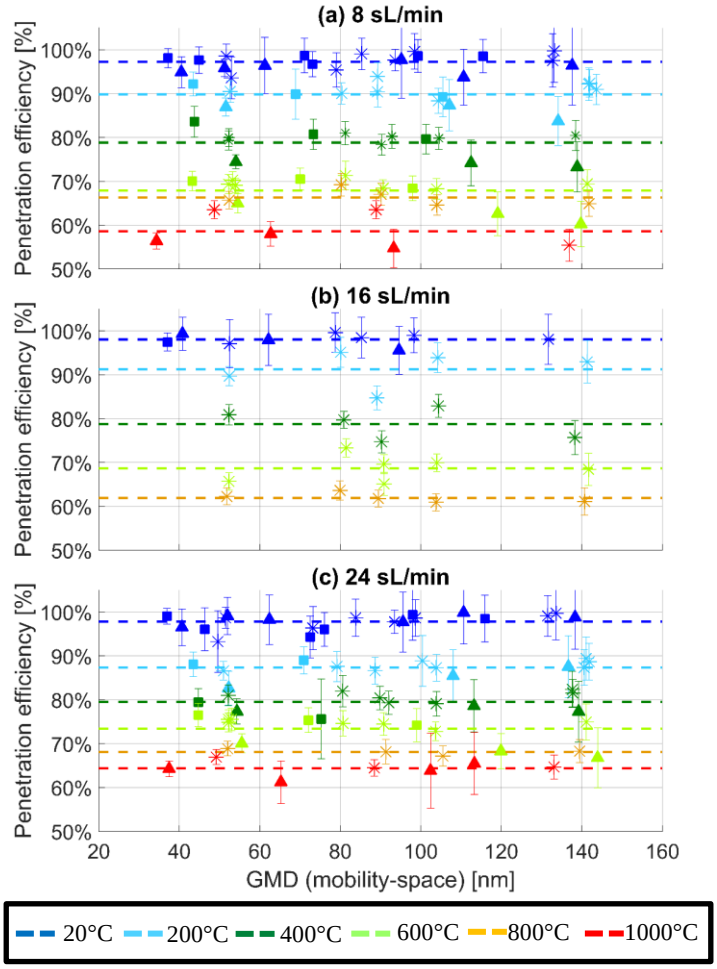

Figure 6: Penetration efficiencies of graphite (Δ), silica (*) and salt (□) particles at various flowrates and furnace temperatures measured with APC (error bars represent ±1 standard deviation of the propagated error of the inlet/outlet 30-second average)

As seen in **Figure 6**, in agreement with previous studies (Lin et al., 2008; Messerer et al., 2003; Muñoz-Bueno et al., 2005), the measured particle penetration efficiencies decrease with increasing furnace temperature relating to higher thermophoretic loss. Conversely, particle size does not appear to impact the measured penetrations at any given temperature/flowrate, as highlighted by the linear regressions fitted at each furnace temperature. As has been previously observed, salt shrinkage to sizes <10 nm was observed at gas temperatures (T_{max}) ≥600°C, which is below the 800°C melting point of NaCl bulk material and can be explained using the theory of evaporation in the free-molecule region (Shimada et al., 1993).

It is also observed that sample flowrate impacts the particle penetration efficiency. As flowrate was shown to display negligible influence on non-thermophoretic loss, during the ambient temperature experiment, it was determined that the flowrate changes resulted in differences in maximum achieved gas temperatures, brought about by changes in residence times. To validate the impact of flowrate on witnessed gas temperature, specific gas temperatures were empirically measured at representative furnace temperatures and flowrates as used in the thermophoretic particle loss experiments (**Figure 7**).

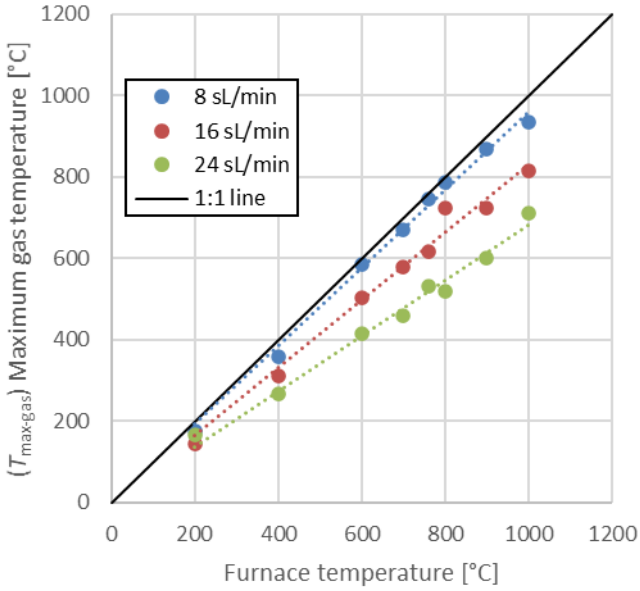

Figure 7: Measured maximum gas temperatures at specific furnace temperatures at representative sample flowrates used in thermophoretic experiments

As thermophoretic particle loss was shown to be independent of particle size (**Figure 6**), average penetration functions were subsequently determined, for each particle type, by averaging all results obtained at each specific flowrate and furnace temperature. These results are presented against the specific gas temperature difference ΔT_{gas} (derived from **Figure 7**) for non-fractal (silica and salt) and fractal (graphite) particles in **Figure 8**. The empirical data is compared to the UTRC and simplified thermophoretic correction factors (Equations **(1&3)**). It is noted that the UTRC predictions and hence k_{thermo} were only originally validated to 160°C using non-fractal particles (Romay et al., 1998), hence have been extrapolated to higher

temperatures (orange dotted line).

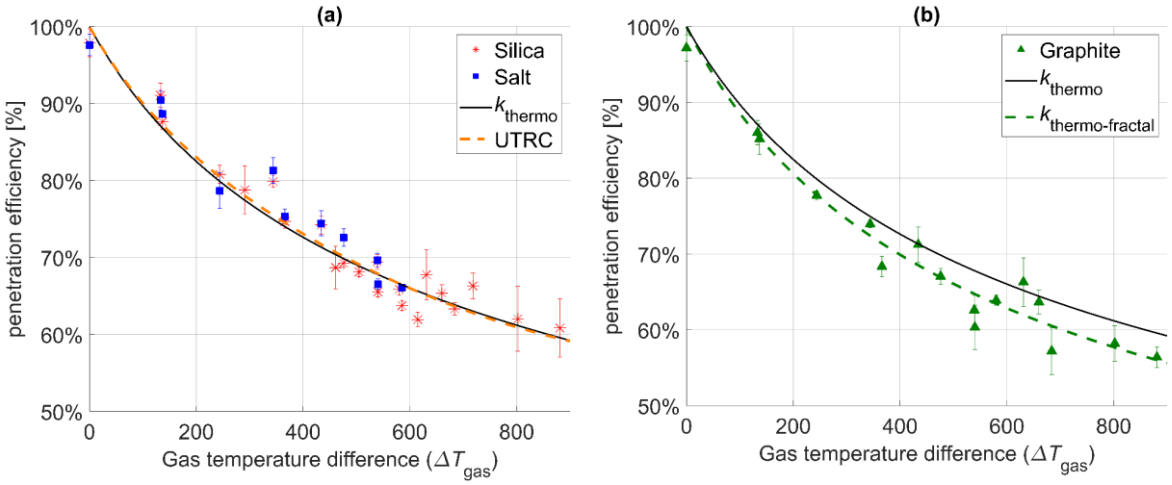

Figure 8: Averaged penetration efficiencies of (a) non-fractal (salt & silica) and (b) fractal (graphite) particles at varying ΔT_{gas} (error bars represent ±1 standard deviation of the averaged penetration efficiency of three AAC sizes)

Again, the penetration efficiencies are observed to decrease with increasing gas temperature gradient, with a largest thermophoretic particle loss of 39.2% measured for non-fractal silica and 43.7% for low-density fractal graphite at ΔT_{gas}=880°C.

In **Figure 8(a)**, the penetration efficiencies of non-fractal salt and silica are seen to show good agreement with one and other and with the predictions of k_{thermo} and UTRC. This is in agreement with previous studies which report that particle material has negligible impact on thermophoretic deposition of non-fractal Ag and TiO_2 particles (8 – 30 nm) (Shimada et al., 1994).

However, it is observed in **Figure 8(b)**, that fractal graphite does not correlate as well with the predictions of k_{thermo}, with larger thermophoretic particle loss observed across the entire temperature range tested (on average 4.1±1.7% lower penetration efficiency compared to non-fractal particles). The higher thermophoretic deposition of graphite suggests that fractal particles composed of multiple primary particles are more strongly affected by thermophoresis as has been previously hypothesized (Rosner and Khalil, 2000), and supported by the larger

thermophoretic velocities (Brugière et al. (2014)) and reduced thermal conductivity (Messerer et al., 2003) reported for aggregate particles. Given the relatively lower particle effective density and mass-mobility exponent of graphite when compared with typical aircraft soot (section **2.1**), the higher thermophoretic loss of ≤4.1% experienced by the fractal graphite may be interpreted as the maximum uncertainty associated with particle morphology for SLT thermophoretic loss predictions and would be represented by a thermophoretic loss factor exponent of 0.43 compared to the 0.38 given in equation **(6)**.

4.3.Bend particle loss quantification

Penetration efficiencies were measured through a 25 m (8 mm ID) antistatic PTFE sample line at a range of particle sizes (30 –140 nm), at three sample flow conditions of 8, 16 and 24 sL/min corresponding to Reynolds numbers of ≈1410, 2820 & 4230. As discussed in section **2.3.2**, specific bend loss was determined by comparing the penetration efficiency measured in the nominally 'straight' 25 m sample line to penetration efficiency measured with the line 'coiled' to the minimal achievable bend radius (11 coils), with the results presented in **Figure 9** & **Figure 10**. The impact of aerosol morphology was again investigated by comparing the penetrations of salt, silica and graphite particles.

It is observed that particle loss in the 'straight' 25 m sample line corresponding to diffusion loss (orange data in **Figure 9**) is ≤20% across all experiments, with the lowest penetration efficiencies reported at laminar conditions (8 sL/min), where particle residence time is the longest, in agreement with previous studies (Sevcenco et al., 2012). It also appears the three particle morphologies display similar diffusion particle loss across the investigated size range. For particles <100 nm, diffusion particle loss is shown to increase with decreasing GMD, in agreement with previous reports (Kumar et al., 2008; Tsai, 2015; Yin and Dai, 2015).

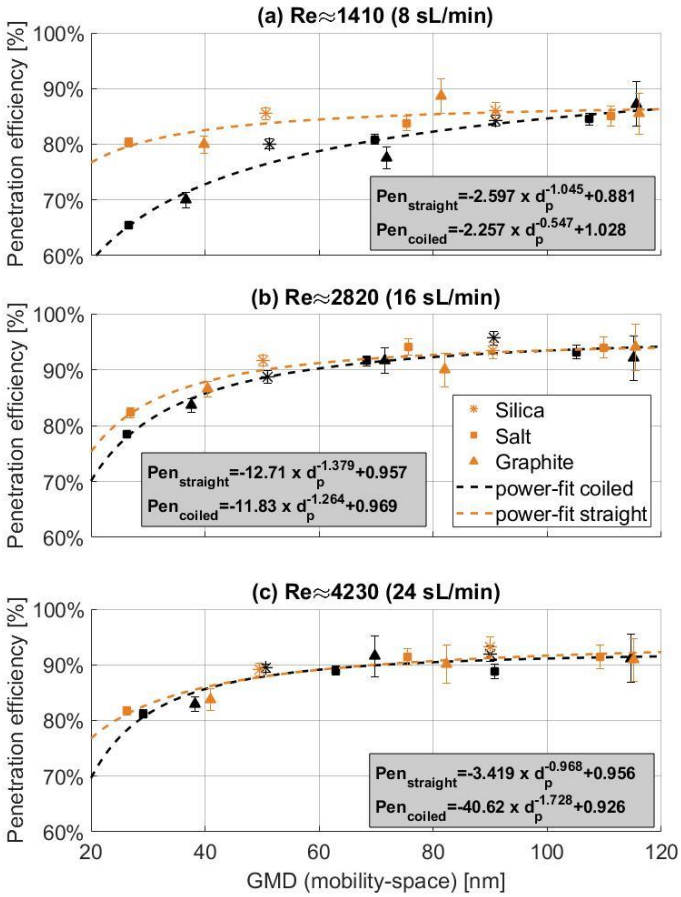

Figure 9: Measured penetration efficiencies of silica, salt and graphite particles in the 'straight and 'coiled' 25 m sample line at various sample flowrates (error bars represent ±1 standard deviation of the propagated error of the inlet/outlet 30-second average)

As the electrical-mobility GMD and GSD of classified particles were seen to temporally fluctuate (**Table 2**), bend loss couldn't be directly deduced from specific measured penetration efficiencies. Instead, the effect of coiling was determined by assessing the relative difference between the 'straight' and 'coiled' power fits ($0.6 \leq R^2 \leq 0.94$) applied to the empirical data (difference between orange & black dashed lines in **Figure 9**). To facilitate visual interpretation, this difference, which represents the measured-derived bend loss, is plotted against UTRC predictions in **Figure 10**.

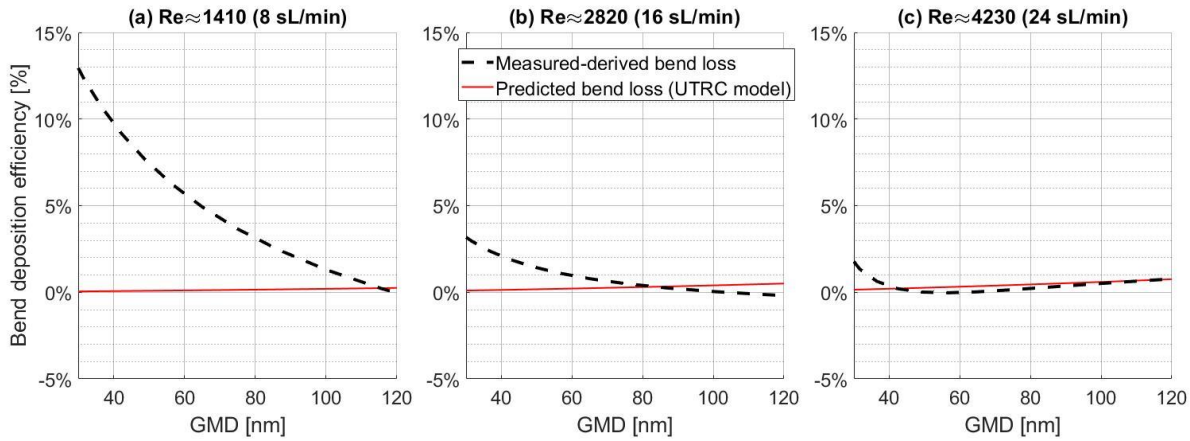

Figure 10: Measured-derived & UTRC model predicted coil induced particle loss at various sample flowrates

Particle loss induced by sample line coiling are observed to decrease with increasing sample flowrate, with reported bend losses ≤13% at 8 sL/min, ≤3% at 16 sL/min and ≤2% at 24 sL/min in the investigated size range. In agreement with previous work, it is suggested that as the sample flowrate increases, the Dean number, defined as the product of Reynold number and the square root of the curvature ratio, increases resulting in reduced bend loss (Yin and Dai, 2015; Yook and Pui, 2006). It was also observed that the morphology of graphite, silica and salt had a negligible impact on bend loss at the investigated conditions.

Bend loss is also seen to generally decrease with increasing GMD at low flowrates. An explanation for this trend is that coiling induces secondary flows, due to centrifugal force, in the bend resulting in particles transporting from the central flow region towards the walls (Wang et al., 2002). This phenomenon enhances diffusion particle loss, which as discussed previously, results in higher losses of smaller particles at lower sample flowrates. As shown by the poor correlations in **Figure 10 (a)&(b)**, this finding is in contradiction with the bend theory as employed by the UTRC model (equations **(4)**&**(5)**) which predicts bend loss to increase with particle size. It is noted that for the conditions and particle sizes investigated in this study, the UTRC model predicts a negligible additional bend loss from the eleven coils (≤1%) which is in

good agreement with the measured-derived bend loss observed at 24 sL/min (**Figure 10 (c)**). Additional work to experimentally characterize diffusion loss in the 10 – 30 nm range for fractal particles at a sample flow of 24 sL/min could identify whether the upturn in **Figure 10 (c)** is an artefact of the power fits. However, to do this, challenges associated with generating and classifying high concentrations of non-volatile fractal particles at this size range need to be overcome.

5. Conclusion

High temperature thermophoretic and bend-induced particle loss were characterized in two test sections using AAC-classified particles of different morphologies (spherical silica, cubical salt and fractal graphite) bounding the upper and lower limits of key aircraft soot morphological properties (i.e. particle effective density, mass-mobility exponent, primary particle size). Laboratory particles were generated at various electrical mobility diameters (30–140 nm) and sampling conditions (8–24 sL/min) relevant to aircraft nvPM regulation.

AAC aerodynamic classification was generally monomodal, with electrical-mobility GMDs ranging from 30–140 nm and GSDs ≥1.23. AAC classification was shown to be dependent on particle morphology and size with classified fractal graphite displaying larger GSDs and being virtually un-classified when selecting an electrical mobility diameter ≤40 nm (corresponding to an equivalent aerodynamic diameter $d_a \leq 20$ nm) due to the prescribed low resolution at the lower size limit of the AAC analyzer (i.e. $d_a = 25$ nm).

Measured particle penetration efficiencies were compared to ICAO proposed particle loss predictions, assessing the effects of particle size and morphology. To the authors knowledge, this empirical data provides unique experimental validation of thermophoretic loss theory for different particle types at $\Delta T_{gas} \leq 880$°C, relevant to current aircraft nvPM sampling loss correction. Thermophoretic particle loss' of up to 43.7% were measured, with higher loss

(≈4.1%) observed for low-density fractal graphite particles when compared to higher density non-fractal particles correlating well with the SLT. The results highlighted that particle morphology had a small but measurable impact on thermophoretic loss, however given the relatively lower density and mass-mobility exponent of graphite when compared with typical aircraft soot, it was concluded that the thermophoretic exponent currently used in the SLT (i.e. 0.38) is representative of aircraft soot, with the experimentally derived uncertainty originating from particle mass-mobility exponent and density (≤4.1%) insignificantly contributing to the overall uncertainty of reported nvPM.

It was demonstrated that the coiling of a 25 m line in compliance with ICAO standards induced negligible additional bend loss at flowrates relevant of aircraft nvPM sampling. However, the current ICAO theory for bend loss does not correlate at lower flowrates, with higher particle loss observed (≤13%) explained by additional diffusion-based particle loss resulting from secondary flows.

These results suggest that current levels of aircraft nvPM uncertainty associated with loss correction for thermophoretic particle loss and sample line coiling are small, with a maximum underprediction of thermophoretic loss ≤4.1% for fractal particles of low effective densities and mass-mobility exponents. Negligible diffusional and inertial particle loss associated with sample line coiling at representative flowrates was observed for particles >30 nm. The observed dependency of particle morphology on aerodynamic classification and thermophoresis highlight that the impact of morphology and the choice of equivalent diameter is critical when defining and characterizing particle loss.

Acknowledgments

This work was a collaborative research program partly funded by Ser Cymru Award NRN123 - National Research Network for Advanced Engineering and Materials, the FLEXIS project

with funding from the Welsh European Funding Office, with support from RAPTOR H2020-EU.3.4.5.10 Clean Sky 2 Joint undertaking under the European Union's Horizon 2020 research and innovation programme (Grant agreement ID: 863969) used to prepare this publication. The authors would also like to acknowledge EASA for the loan of the EU nvPM mobile reference system under contract EASA.2015.C01.AM01.

References

Baron, P., Willeke, K., and Kulkarni, P. (2011). Aerosol Measurement, Principles, Techniques, and applications (John Wily & Sons, Inc).

Biskos, G., Reavell, K., and Collings, N. (2005). Description and Theoretical Analysis of a Differential Mobility Spectrometer. Aerosol Science and Technology *39*, 527–541.

Boies, A.M., Stettler, M.E.J., Swanson, J.J., Johnson, T.J., Olfert, J.S., Johnson, M., Eggersdorfer, M.L., Rindlisbacher, T., Wang, J., Thomson, K., et al. (2015). Particle Emission Characteristics of a Gas Turbine with a Double Annular Combustor. Aerosol Science and Technology *49*, 842–855.

Brugière, E., Gensdarmes, F., Ouf, F.X., Yon, J., and Coppalle, A. (2014). Increase in thermophoretic velocity of carbon aggregates as a function of particle size. Journal of Aerosol Science *76*, 87–97.

Cambustion Ltd (2016). Aerodynamic Aerosol Classifier - User manual (V1.12).

Charvet, A., Bau, S., Paez Coy, N.E., Bémer, D., and Thomas, D. (2014). Characterizing the effective density and primary particle diameter of airborne nanoparticles produced by spark discharge using mobility and mass measurements (tandem DMA/APM). J Nanopart Res *16*, 2418.

Cheng, M.-D., Storey, J.M., Wainman, T., and Dam, T. (2002). Impacts of venturi turbulent mixing on the size distributions of sodium chloride and dioctyl-phthalate aerosols. Journal of Aerosol Science *33*, 491–502.

Crane, R.I., and Evans, R.L. (1977). Inertial deposition of particles in a bent pipe. Journal of Aerosol Science *8*, 161–170.

Crayford, A., and Johnson, M. (2012). SAMPLE III SC.02 - Studying, sAmpling and Measuring of aircraft ParticuLate Emission (EASA).

Crayford, A., and Johnson, M. (2013). SAMPLE III SC.03- Studying, sAmpling and Measuring of aircraft ParticuLate Emission (EASA).

Delhaye, D., Ouf, F.-X., Ferry, D., Ortega, I.K., Penanhoat, O., Peillon, S., Salm, F., Vancassel, X., Focsa, C., Irimiea, C., et al. (2017). The MERMOSE project: Characterization of particulate matter emissions of a commercial aircraft engine. Journal of Aerosol Science *105*, 48–63.

Durand, E. (2019). Towards improved correction methodology for regulatory aircraft engine nvPM measurement. Thesis (PhD). Cardiff University.

Durdina, L., Brem, B.T., Abegglen, M., Lobo, P., Rindlisbacher, T., Thomson, K.A., Smallwood, G.J., Hagen, D.E., Sierau, B., and Wang, J. (2014). Determination of PM mass emissions from an aircraft turbine engine using particle effective density. Atmospheric Environment *99*, 500–507.

Fissan, H., Ristig, S., Kaminski, H., Asbach, C., and Epple, M. (2014). Comparison of different characterization methods for nanoparticle dispersions before and after aerosolization. Analytical Methods *6*, 7324–7334.

Fushimi, A., Saitoh, K., Fujitani, Y., and Takegawa, N. (2019). Identification of jet lubrication oil as a major component of aircraft exhaust nanoparticles. Atmospheric Chemistry and Physics *19*, 6389–6399.

Giechaskiel, B. (2012). Sampling of Non-Volatile Vehicle Exhaust Particles: A Simplified Guide.

Giechaskiel, B., Ntziachristos, L., and Samaras, Z. (2009). Effect of ejector dilutors on measurements of automotive exhaust gas aerosol size distributions. Meas. Sci. Technol. *20*, 045703.

Gysel, M., Laborde, M., Mensah, A.A., Corbin, J.C., Keller, A., Kim, J., Petzold, A., and Sierau, B. (2012). Technical Note: The single particle soot photometer fails to reliably detect PALAS soot nanoparticles. Atmospheric Measurement Techniques *5*, 3099–3107.

Hagen, D.E., Lobo, P., Whitefield, P.D., Trueblood, M.B., Alofs, D.J., and Schmid, O. (2009). Performance Evaluation of a Fast Mobility-Based Particle Spectrometer for Aircraft Exhaust. Journal of Propulsion and Power *25*, 628–634.

Hinds, W.C. (1998). Aerosol Technology: Properties Behavior, and measurement of airborne particles (Wiley-Interscience).

ICAO (2017). Annex 16 - Environmental Protection Volume 2 - Aircraft Engine Emissions.

Jeon, S., R. Oberreit, D., Van Schooneveld, G., and Hogan, C. (2016). Nanomaterial Size Distribution Analysis via Liquid Nebulization Coupled with Ion Mobility Spectrometry (LN-IMS). The Analyst *141*.

Johnson, T.J., Irwin, M., Symonds, J.P.R., Olfert, J.S., and Boies, A.M. (2018). Measuring aerosol size distributions with the aerodynamic aerosol classifier. Aerosol Science and Technology *52*, 655–665.

Jonsdottir, H.R., Delaval, M., Leni, Z., Keller, A., Brem, B.T., Siegerist, F., Schönenberger, D., Durdina, L., Elser, M., Burtscher, H., et al. (2019). Non-volatile particle emissions from aircraft turbine engines at ground-idle induce oxidative stress in bronchial cells. Communications Biology *2*, 90.

Kittelson, D.B. (1998). Engines and nanoparticles: a review. Journal of Aerosol Science *29*, 575–588.

Kreith, F., Manglik, R.M., and Bohn, M.S. (2012). Principles of Heat Transfer, SI Edition (Cengage Learning).

Kumar, P., Fennell, P., Symonds, J., and Britter, R. (2008). Treatment of losses of ultrafine aerosol particles in long sampling tubes during ambient measurements. Atmospheric Environment *42*, 8819–8826.

Lin, J.-S., Tsai, C.-J., Tung, K.-L., and Chiang, H.-C. (2008). Thermophoretic particle deposition efficiency in turbulent tube flow. Journal of the Chinese Institute of Chemical Engineers *39*, 281–285.

Lobo, P., Hagen, D.E., Whitefield, P.D., and Raper, D. (2015a). PM emissions measurements of in-service commercial aircraft engines during the Delta-Atlanta Hartsfield Study. Atmospheric Environment *104*, 237–245.

Lobo, P., Durdina, L., Smallwood, G.J., Rindlisbacher, T., Siegerist, F., Black, E.A., Yu, Z., Mensah, A.A., Hagen, D.E., Miake-Lye, R.C., et al. (2015b). Measurement of Aircraft Engine Non-Volatile PM Emissions: Results of the Aviation-Particle Regulatory Instrumentation Demonstration Experiment (A-PRIDE) 4 Campaign. Aerosol Science and Technology *49*, 472–484.

Lobo, P., Durdina, L., Brem, B.T., Crayford, A.P., Johnson, M.P., Smallwood, G.J., Siegerist, F., Williams, P.I., Black, E.A., Llamedo, A., et al. (2020). Comparison of standardized sampling and measurement reference systems for aircraft engine non-volatile particulate matter emissions. Journal of Aerosol Science 105557.

Lyyränen, J., Jokiniemi, J., Kauppinen, E.I., Backman, U., and Vesala, H. (2004). Comparison of Different Dilution Methods for Measuring Diesel Particle Emissions. Aerosol Science and Technology *38*, 12–23.

Masiol, M., and Harrison, R.M. (2014). Aircraft engine exhaust emissions and other airport-related contributions to ambient air pollution: A review. Atmospheric Environment *95*, 409–455.

Messerer, A., Niessner, R., and Pöschl, U. (2003). Thermophoretic deposition of soot aerosol particles under experimental conditions relevant for modern diesel engine exhaust gas systems. Journal of Aerosol Science *34*, 1009–1021.

Muñoz-Bueno, R., Hontañón, E., and Rucandio, M.I. (2005). Deposition of fine aerosols in laminar tube flow at high temperature with large gas-to-wall temperature gradients. Journal of Aerosol Science *36*, 495–520.

Olfert, J., and Rogak, S. (2019). Universal relations between soot effective density and primary particle size for common combustion sources. Aerosol Science and Technology *53*, 485–492.

PALAS GmbH Operating Manual Graphite Aerosol Generator GFG 1000.

Park, J.Y., McMurry, P.H., and Park, K. (2012). Production of Residue-Free Nanoparticles by Atomization of Aqueous Solutions. Aerosol Science and Technology *46*, 354–360.

Park, K., Kim, J.-S., and Miller, A.L. (2009). A study on effects of size and structure on hygroscopicity of nanoparticles using a tandem differential mobility analyzer and TEM. J Nanopart Res *11*, 175–183.

Petzold, A., Marsh, R., Johnson, M., Miller, M., Sevcenco, Y., Delhaye, D., Ibrahim, A., Williams, P., Bauer, H., Crayford, A., et al. (2011). Evaluation of Methods for Measuring Particulate Matter Emissions from Gas Turbines. Environ. Sci. Technol. *45*, 3562–3568.

Pui, D.Y.H., Romay-Novas, F., and Liu, B.Y.H. (1987). Experimental Study of Particle Deposition in Bends of Circular Cross Section. Aerosol Science and Technology *7*, 301–315.

Romay, F.J., Takagaki, S.S., Pui, D.Y.H., and Liu, B.Y.H. (1998). Thermophoretic deposition of aerosol particles in turbulent pipe flow. Journal of Aerosol Science *29*, 943–959.

Rosner, D.E., and Khalil, Y.F. (2000). Particle morphology- and knudsen transition-effects on thermophoretically dominated total mass deposition rates from "coagulation-aged" aerosol population. Journal of Aerosol Science *31*, 273–292.

SAE international (2017). AIR 6504 - Procedure for the Calculation of Sampling System Penetration Functions and System Loss Correction Factors.

SAE international (2018). ARP 6320 - Procedure for the Continuous Sampling and Measurement of Non-Volatile Particulate Matter Emissions from Aircraft Turbine Engines.

SAE international (2019). ARP 6481- Procedure for the Calculation of Sampling Line Penetration Functions and Line Loss Correction Factors (SAE International).

Saffaripour, M., Thomson, K.A., Smallwood, G.J., and Lobo, P. (2019). A Review on the Morphological Properties of Non-volatile Particulate Matter Emissions from Aircraft Turbine Engines. Journal of Aerosol Science 105467.

Sevcenco, Y.A., Walters, D., Crayford, A.P., Marsh, R., Bowen, P.J., and Johnson, M.P. (2012). Evaluation of Transport Line Effects on PM Size Distribution for Aircraft Exhaust for Different Flow Regimes and Dilution Methodology. 1125–1133.

Shimada, M., Seto, T., and Okuyama, K. (1993). Thermophoretic and evaporational losses of ultrafine particles in heated flow. AIChE J. *39*, 1859–1869.

Shimada, M., Seto, T., and Okuyama, K. (1994). Wall Deposition of Ultrafine Aerosol Particles by Thermophoresis in Nonisothermal Laminar Pipe Flow of Different Carrier Gas. Jpn. J. Appl. Phys. *33*, 1174.

Steiner, S., Bisig, C., Petri-Fink, A., and Rothen-Rutishauser, B. (2016). Diesel exhaust: current knowledge of adverse effects and underlying cellular mechanisms. Arch Toxicol *90*, 1541–1553.

Tavakoli, F., and Olfert, J.S. (2013). An Instrument for the Classification of Aerosols by Particle Relaxation Time: Theoretical Models of the Aerodynamic Aerosol Classifier. Aerosol Science and Technology *47*, 916–926.

Tavakoli, F., Symonds, J.P.R., and Olfert, J.S. (2014). Generation of a Monodisperse Size-Classified Aerosol Independent of Particle Charge. Aerosol Science and Technology *48*, i–iv.

Tsai, C.S.-J. (2015). Characterization of Airborne Nanoparticle Loss in Sampling Tubing. Journal of Occupational and Environmental Hygiene *12*, D161–D167.

Tsai, C.-J., Lin, J.-S., Aggarwal, S.G., and Chen, D.-R. (2004). Thermophoretic Deposition of Particles in Laminar and Turbulent Tube Flows. Aerosol Science and Technology *38*, 131–139.

Wang, J., Flagan, R.C., and Seinfeld, J.H. (2002). Diffusional losses in particle sampling systems containing bends and elbows. Journal of Aerosol Science *33*, 843–857.

Weichenthal, S., Olaniyan, T., Christidis, T., Lavigne, E., Hatzopoulou, M., Van Ryswyk, K., Tjepkema, M., and Burnett, R. (2019). Within-City Spatial Variations in Ambient Ultrafine Particle Concentrations and Incident Brain Tumors in Adults. Epidemiology *Publish Ahead of Print*.

Yin, Z., and Dai, Z. (2015). Investigating the Nanoparticles Penetration Efficiency through Horizontal Tubes Using an Experimental Approach. Advances in Mathematical Physics.

Yook, S.-J., and Pui, D.Y.H. (2006). Experimental Study of Nanoparticle Penetration Efficiency Through Coils of Circular Cross-Sections. Aerosol Science and Technology *40*, 456–462.

Zhang, X., Chen, X., and Wang, J. (2019). A number-based inventory of size-resolved black carbon particle emissions by global civil aviation. Nat Commun *10*, 1–11.